

1 UAV video-based estimates of nearshore bathymetry

2 Athina M.Z. Lange^{a,*}, Julia W. Fiedler^a, Mark A. Merrifield^a and R. T. Guza^a

3 ^aScripps Institution of Oceanography, La Jolla, CA, USA

4 ARTICLE INFO

5 **Keywords:**
6 Bathymetry
7 Remote sensing
8 Machine learning
9 UAV

ABSTRACT

Nearshore bathymetry estimated from video acquired by a hovering UAV is compared with ground truth. Bathymetry estimates from the widely used cBathy algorithm are improved by crest tracking (with machine learning) from near breaking through the surf zone. Individual wave crests (distinguished from the breaking wave toe that can move down the wave front face) in video timestamp stacks are determined with a deep-learning neural network and surf zone depth estimates are computed from the wave celerity. Time-2D spatial transforms (cBathy) are used to estimate wave celerity and depth between the surf zone and 10-m depth. Composite profiles (cBathyCT), formed by joining cBathy and crest-tracking solutions near the surf zone seaward edge, based on a newly determined $\gamma(x)$ parameter, avoid the large cBathy errors associated with the onset of breaking. Incident wave heights were relatively constant on each day but varied over days between 0.55–2.15m. Averaged over all 17 min hovers and cross-shore transects (112 total), surf zone depths errors were relatively small (average root-mean-square error $\langle \text{RMSE} \rangle = 0.17\text{m}$, $\langle \text{Bias} \rangle = 0.06\text{m}$) after including a heuristic nonlinear correction to the linear phase speed. Between the seaward surf zone edge and 10m depth, errors are similar to previous cBathy studies: $\langle \text{RMSE} \rangle = 0.87\text{m}$, $\langle \text{Bias} \rangle = 0.58\text{m}$ with the largest errors in deepest water. Beach profiles were generally similar for all 8 test days, concave up with a slight terrace (no sandbar) and small alongshore depth variations. Accuracy was lower on one transect with a shallow reef.

1. Introduction

Accurate bathymetry is critical to understanding nearshore processes like beach erosion and accretion, the fate of beach nourishment sand, sandbar migration, and the corresponding hydrodynamics. While topography above the waterline may be monitored efficiently with mobile scanning LiDAR or photogrammetry, subaqueous nearshore bathymetry is usually less well-known owing to the expense of insitu subaqueous surveys. Early-warning overtopping forecasts can therefore have limited accuracy owing to over-simplified (planar) or outdated bathymetry (Stephens and Cloke, 2014; Stokes et al., 2019; Jordi et al., 2019; Stokes et al., 2021; Merrifield et al., 2021; USGS, 2022; Gomes da Silva et al., 2020, and references therein).

Remote sensing via satellite or video can provide relatively wide-area, low-cost observations of nearshore bathymetry. Satellite subaqueous observations require relatively clear water, and resolution in space and time can be limited (Vanderstraete et al., 2003; Mallet and Bretar, 2009; Jing and Datt, 2010; Abileah and Trizna, 2010; Gao, 2009; Zuckerman and Anderson, 2018; Legleiter and Harrison, 2019; Li et al., 2019; Geyman and Maloof, 2019). Enabled by improved cameras and computing power, nearshore bathymetry can be estimated using video observations of surface wave dissipation and celerity (Holman and Haller, 2013). Wave dissipation methods use high-intensity peaks in time-averaged images (timex e.g. ARGUS stations (5-camera system, Holman and Stanley, 2007)) to identify persistent foam caused by depth-limited breaking on sandbar crests (Lippmann and Holman, 1989; Aarninkhof, 2005; Collins et al., 2020). Celerity-based methods exploit the dependence of wave celerity on depth (Stockdon and Holman, 2000; Plant et al., 2009; Holman et al., 2013; Rutten et al., 2017; Radermacher et al., 2014; Holman and Haller, 2013; Wengrove et al., 2013; Bergsma et al., 2016; Catálan and Haller, 2008; Almar et al., 2009; Thuan et al., 2019; Tsukada et al., 2020).

The accuracy of estimated depths can be improved with prior imagery from long-term observations and sophisticated numerical modeling. Observed and numerical model predictions of wave dissipation patterns can be coupled and used in data-assimilation schemes that estimate depth from pixel intensity, wave celerity and other observables

*This document is the results of the research project funded by the U.S. Army Corps of Engineers and the California Department of Parks and Recreation.

*Corresponding author

✉ alange@ucsd.edu (A.M.Z. Lange)

ORCID(s): 0000-0002-7650-9976 (A.M.Z. Lange); 0000-0002-4797-8933 (J.W. Fiedler)

(Aarninkhof, 2005; van Dongeren et al., 2008). Full end-to-end machine learning methods combine image analysis with extensive past bathymetry observations and sophisticated wave modeling (Collins et al., 2020).

Bathymetry is often required in areas lacking continuous, long-term observations, and the fixed, elevated platform for a permanent camera system. To address this, hovering UAVs (Uncrewed Aerial Vehicles) have increasingly been used for nearshore observations (Brodie et al., 2019). In this study, we evaluate the accuracy of bathymetry estimates obtained from relatively short (17-minute) observations taken from a hovering UAV, without use of prior imagery, bathymetry surveys, or numerical wave models. We use celerity and the proportion of waves breaking in relation to cross-shore location to refine depth estimates in the outer surf zone, where the mix of both broken and unbroken creates errors in existing methods.

Bathymetry is estimated in four steps: 1) cBathy is applied offshore of the surf zone, 2) timestack images are used to track individual wave crests and locate the onset of breaking. Crests are tracked with a deep learning U-Net algorithm, 3) surf zone depth is estimated using the observed crest celerity and shallow water theory with a simple nonlinear correction and 4) full depth profiles (from backbeach to 8m depth) combine cBathy offshore, crest tracking in the surf zone, and a low-tide survey of the subaerial beach.

In Section 2, existing video-based estimates of bathymetry are reviewed and extended. Observations are described in Section 3. In Section 4, methods valid within and seaward of the surf zone are combined, yielding composite profiles that are then compared with ground truth bathymetric surveys. Error sources and the need for additional model development to include complex bathymetry are discussed in Section 5.

2. Background

2.1. cBathy

cBathy (Holman et al., 2013; Holman and Bergsma, 2021) is a popular, open-source celerity-based depth inversion algorithm. It fits the most coherent frequency-wavenumber pairs (default of 4) to the cross-spectra of all pixels within a given area around a point. The depth estimates are based on the nonlinear best fit from the dominant frequency-wavenumber pairs from the surrounding points and the linear dispersion relationship (see Table 2 for cBathy parameters used here). cBathy $\langle \text{RMSE} \rangle$ (average root-mean-square-error) of individual estimates are $\sim 0.72\text{m}$ with low waves ($H < 1.2\text{m}$) and 1.28m with all H included (Brodie et al., 2018; Holman and Bergsma, 2021; Wengrove et al., 2013; Bergsma et al., 2019; Rodríguez-Padilla et al., 2022). The offshore extent of accurate cBathy depends on camera quality, elevation, and stabilization (particularly for UAVs, Bergsma et al., 2019); insitu validation is limited to $< 7\text{m}$ depth at the Field Research Facility (FRF) in Duck, NC, USA, and reasonably good agreement ($\langle \text{RMSE} \rangle = 0.56\text{m}$, $\langle \text{Bias} \rangle = -0.41\text{m}$) between cBathy and observations as deep as 14m were obtained at Agate Beach, Oregon, USA using an elevated (128m) headland-mounted camera (Holman et al., 2013). Results here extend to 10m depth, about 500m from the backbeach.

cBathy assumes spatially homogeneous waves and bathymetry over a specified tile size (here we use 50m cross-shore by 200m alongshore, Figure 1). Prior to wave breaking, wave front faces usually appear darker than wave rear faces. However, when waves begin breaking, the foam-dominated front wave face becomes much brighter (whiter) than the back face, reversing the pattern from offshore. Switching between dark and light wave faces within a tile can cause large celerity and depth overestimates and is known as the Modulation Transfer Function (MTF). Holman et al. (2013) suggests using the shifting cross-shore location of the “switching region” over a tidal cycle (or longer) and a Kalman filter to reduce these errors. Kalman results accumulate over a series of prior data collections, with each new run improving the estimate until the results stabilize after roughly one or two days (Holman and Bergsma, 2021). Alternatively, Bergsma et al. (2019) used the absolute value of the pixel intensity time derivative to augment timestacks and reduce foam on the image. This modified signal is included in the input data for cBathy and reduces the surf zone $\langle \text{RMSE} \rangle$ from 3.1m to 1.3m . Here, surf zone depths are inferred from 17-min timestacks of individual waves (Figure 1 c,d), without Kalman filtering.

2.2. Timestack Analysis

Timestack images (Figure 1 c,d) show wave evolution over time on a single cross-shore transect, rather than snapshots of a 2D field (Figure 1 a,b). The x-location of individual shoaling and breaking waves can be determined in sequential pixel columns. Depth estimates based on video celerity are necessarily heuristic. The relationship between pixel intensity and sea surface elevation is a required assumption (Lippmann and Holman, 1991). Many RGB image-based timestack analyses use standard edge detection algorithms (Canny or Sobel, Szeliski, 2022) to identify

the wave toe, the bright front edge of the incoming, breaking waves that sharply contrast with the darker water in front. However, as spilling breaking begins and the roller slides down the wave face, the toe moves faster than the crest, increasing the estimated speed and complicating depth inversions. The roller toe eventually reaches a relatively stable position on the wave face, and in the inner surf zone is a stable proxy for the wave crest (Stive, 1980; Basco, 1985; Svendsen et al., 2003). Traditional computer vision approaches have difficulty detecting wave crests (as opposed to toes) robustly inside the surf zone due to the complexity of foam patterns (Stringari et al., 2019). Yoo et al. (2011) combined Radon-transform edge tracking and a nonlinear wave propagation model to estimate shallow water ($h < 2\text{m}$) bathymetry accurately ($\langle \text{RMSE} \rangle = 0.25\text{m}$, $\langle \text{Bias} \rangle = 0.1\text{m}$) with relatively low incident wave heights ($H < 0.8\text{m}$) on bathymetry not dissimilar to Torrey Pines State Beach, CA, USA (our primary study site). Stringari et al. (2019) estimates phase speed using a combination of Sobel edge detection, pixel-intensity extrema, and machine learning to extract the white signature of ‘foam corresponding to the crests of breaking waves’ with surf zone wave heights and depths less than 1m.

We were unable to implement Stringari et al. (2019), Yoo et al. (2011), and Bergsma et al. (2019) with the present observations. Almar et al. (2009) and Tsukada et al. (2020) obtain mean wave celerity using a cross-correlation technique with varying space and time intervals. However, for a test case, the correlation methods were relatively noisy for the present data and still exhibit the well-known errors in the breakpoint transition zone (not shown). Here we describe an alternative and reproducible crest-tracking algorithm with good surf zone performance, available in a GitHub repository. A crest-tracking algorithm with good surf zone performance with H_s as large as 2m in 4m depth is described and combined with cBathy estimates valid offshore and a low-tide subaerial survey to obtain a full nearshore profile.

2.3. Surf Zone Wave Celerity

In linear (small amplitude) shallow water theory waves advance with celerity

$$c = \sqrt{gh}. \quad (1)$$

However, nonlinear shoaling and breaking waves travel with amplitude-dependent phase speeds faster than c (Svendsen and Buhr Hansen, 1976; Svendsen et al., 2003). For idealized cnoidal and solitary waves with wave height H

$$c^2 = g(h + H) = gh(1 + H/h), \quad (2)$$

(Inman et al., 1971; Thornton and Guza, 1982; Stockdon and Holman, 2000). Assuming a saturated surf zone with $\gamma = H_{rms}/h$ yields

$$h_{estimate} = c^2/(g(1 + \gamma)). \quad (3)$$

surf zone waves are not constant shape as assumed in (2). Although phase speeds for nonlinear random waves generally increase with increasing amplitude, (3) is a heuristic simplification.

Variations in observed γ between 0.3 and 1.1 have been ascribed to the effects of beach slope, breaker wave type (e.g. plunging versus spilling) and location within the surf zone (Raubenheimer et al., 1996; Catálan and Haller, 2008; Brodie et al., 2018). For both broken and unbroken waves, c on average increases with increasing amplitude and depth but celerity observed on a wave-by-wave basis diverges from Eq. 3. Despite these complications, corrections based on Eq. 3 consistently improve celerity-based surf zone depth estimates (Holland, 2001; Svendsen et al., 2003; Catálan and Haller, 2008; Yoo et al., 2011; Tissier et al., 2015; Fiedler et al., 2021; Martins et al., 2018). We compare observed depths with estimates from linear (Eq. 1) and simplified nonlinear (Eq. 3) crest-tracking methods.

3. Observations

We completed 52 UAV hovers in San Diego, California with a DJI Phantom 4 RTK drone: 39 hovers over 6 days at Torrey Pines State Beach (July 2020 - Dec 2021), 6 hovers during 1 day at Cardiff State Beach, and 7 hovers over 1 day at Scripps Institution of Oceanography (SIO). Wave conditions were relatively constant during data collection on each day, and varied over the 8 days, with $0.55 < H_0 < 2.15\text{m}$ and $9 < T_p < 17.6\text{s}$ (Table 1). Transects are defined by MOnitoring and Prediction (MOP) System number (O'Reilly et al., 2016). Torrey Pines depth varies little alongshore with a maximum difference of approximately 1m across 300–500m (Figure 2 a insert). Bathymetries at the three sites are similar, with the exception of a pronounced bedrock reef on MOP 667 at Cardiff and a well-developed

Date	Location	Hovers (MOP transect)	H_s (m)	T_p (s)	Obliquity (degree)	Tide Range (NAVD88m)
Jul 07, 2020	Torrey Pines	13 (579 - 584)	0.89	11.3	-12	-0.27 - 1.13
Oct 10, 2020	Scripps	7 (513 - 514)	0.55	9	14	0.22 - 0.8
Jul 09, 2021	Cardiff	6 (670 - 667)	0.8	16.7	-21.5	0.28 - 0.9
Jul 12, 2021	Torrey Pines	6 (581 - 584)	0.7	10	7	-0.06 - 0.41
Oct 26, 2021	Torrey Pines	5 (581 583)	2.15	17.7	1	1.07 - 1.26
Nov 02, 2021	Torrey Pines	5 (581 583)	1.12	16.7	6	0.1 - 0.72
Dec 02, 2021	Torrey Pines	5 (581 583)	0.65	12.3	2	-0.22 - 0.49
Dec 15, 2021	Torrey Pines	5 (581 583)	1.96	15.4	-4	0.8 - 1.4

Table 1

UAV flight info and wave conditions from MOP forecasts in 10m depth. Incident wave parameters include significant wave height H_s , peak period T_p , and obliquity relative to beach normal.

140 terrace at SIO (Figure 2). The beach profile near and above the waterline was measured with subaerial (LiDAR or
141 photogrammetry) beach surveys on the same day as UAV hovers.

142 UAV hovers were typically 17 min (minimum 10 min). The UAV hovered between 27 and 91.5m above NAVD88,
143 with no significant difference in performance with height. JPEG images were extracted from the video using the
144 ffmpeg tool at 10Hz. RTK-surveyed, 1m x 1m checkerboards provide stability control points used for rectification
145 with CIRN UAV Rectification software (Bruder and Brodie, 2020). Cross-shore timestampacks were extracted at 20m
146 along-shore intervals, gridded up to 500m offshore at 0.1m spacing. The (dx, dt) size was kept constant across all
147 extracted timestampacks and is a trained part of the neural network.

148 Ground truth was insitu (labor-intensive) bathymetry surveys (jet ski, push dolly, All-Terrain Vehicle) on 100-m
149 alongshore intervals to 10m depth usually obtained on the same day as the hovers, and always within one day. There
150 were usually 3 cross-shore transects within the video field of view (Table 1), although the number varied with different
151 video look angles. The 52 hovers included a total of 11 unique surveyed transects at 3 sites, with a total of 112 transects
152 with ground truth.

153 4. Methods

154 Our proposed method combines an existing celerity-based depth inversion algorithm (cBathy 2.0, Holman et al.,
155 2013; Holman and Bergsma, 2021), which has been shown to be most effective seaward of the surf zone, with non-
156 linear surf zone depth estimates derived from machine learning-aided timestampack wave crest tracks. The method is
157 implemented in four steps.

158 4.1. cBathy Surf Zone Depth Estimation

159 cBathy results based on a single hover (no Kalman filtering) have much larger RMSE in the surf zone than off-
160 shore, similar to Holman et al. (2013); Brodie et al. (2018); Bergsma et al. (2019) and others. Holman and Bergsma
161 (2021) consider cBathy estimates unreliable when the cBathy 95% confidence interval $hErr > 0.5$. This criterion
162 can underestimate the width of the overpredicted data (Figure 3 a) or fail to identify a narrow surf zone (Figure 3 b)
163 resulting in $\langle RMSE \rangle$ and $\langle Bias \rangle > 0.8m$. A constant threshold other than $hErr > 0.5$ did not reliably estimate where
164 cBathy failed. An alternative criterion assumes that cBathy estimates are corrupted by a mix of breaking (white faced)
165 and nonbreaking (dark faced) waves. The fraction of waves breaking (determined from timestampacks, below) defines the
166 region of cBathy validity as $> 95\%$ (inner surf zone) or $< 5\%$ (offshore) of waves breaking (Figure 3 e,f), and can be
167 used instead of the standard $hErr > 0.5$ as the region where cBathy fails. In addition, the fraction of wave breaking can
168 also be used to determine a nonlinear correction (described in Section 4.3) to include in the cBathy estimates. For all 3
169 error-filtered cBathy versions (only using $hErr < 0.5$, removing timestampack derived wave-breaking region, and nonlinear
170 correction to cBathy), estimates are interpolated across regions where cBathy fails (according to the different criteria,
171 Figure 3).

172 4.2. Deep Learning for Timestampack-image Wave Crest Detection

173 Traditional computer vision techniques, e.g. Canny or Sobel edge detection, often have difficulty accurately iden-
174 tifying the location of wave crests when foam is persistent (Stringari et al., 2019). Because manually identifying wave
175 crests (e.g. through ground-truth annotations) can be time-consuming, we propose using a deep learning approach as

Parameter	Description	Value
Δt	Time series sampling interval	0.5s
$(\Delta x_p, \Delta y_p)$	Pixel spacing	(5,5)m
$(\Delta x_m, \Delta y_m)$	Analysis point spacing	(5,25)m
(h_{min}, h_{max})	Min/Max acceptable depth	(0.25, 20)m
(L_x, L_y)	Analysis smoothing scale	(25,100)m
κ	Smoothing scale expansion at outer boundary	3
f	Analysis frequency bins, range and df	[0.055 – 0.25 : 0005] Hz
N_{keep}	Number of frequency bins to retain	4

Table 2

cBathy 2.0 Parameters (Holman and Bergsma, 2021)

an automated annotation tool (e.g. Collins et al., 2020). Our method is not intended to provide new information, but rather to aid in the tedious process of identifying wave crests, which we define as the location between the solid block of white water that is characteristic of a wave roller and the more interspersed longer tracks of foam on the back side of a broken wave (Figure 4 insert).

The training/validation dataset consists of 20 timestamp-images with sparse (not for all waves) ground-truth provided by binary hand annotations of wave crests. To include a range of wave, lighting, and bathymetry conditions, one transect from each hover in Fall 2021 at Torrey Pines is included. Training used 16 randomly selected timestamp-images and validation used 4. Note that because the deep learning approach is used here simply as an annotation tool, the specific choices of parameters of the neural network are of little importance.

Figure 4 shows the workflow for the crest-detection. An input timestamp is provided and a binary output image of the detected crests is returned. An example of the output wave crests superimposed on the timestamp image can be seen in the insert. Further details on the wave crest detection algorithm can be found in Appendix A.

4.3. Surf Zone Depth from Crest-tracking

The surf zone method estimates the celerity of individual wave crests observed in timestamp stacks using a deep learning neural network. Depth is recovered by inverting celerity using linear and nonlinear shallow water dispersion.

Crest tracks are extracted from U-Net binary output images (Figure 4). The 2-D binary image is reduced to 1-pixel (0.1 m, 0.1 sec) wide curves, and the (x, t) coordinates of the individual curves are detected by 1) finding the first offshore instance of the curve (where no other black points are found previously in time and further offshore in a given area), 2) following the crest, with the next coordinate detected by the shortest Euclidean distance between black points that follow in time and are onshore of the current points, and 3) removing short curves (< 7.5 sec). Figure 1 c,d shows the difference between the initial U-Net output and the wave crests accepted for computing celerity. The phase speed of each crest, computed by the best-fit slope (RANSAC) between two points in the 15m vicinity of each (x, t) coordinate along the curve, is interpolated onto a regular grid of 0.1m intervals. The same gridding discretization (0.1 m, 0.1 sec) is used everywhere. At large offshore distances, a single video pixel can span multiple grid points, resulting in degraded accuracy. To address this issue, a pixel resolution cutoff is applied. Any pixel that covers more than 2 grid points is removed.

The ‘breakpoint transition’ (BP) method uses linear and nonlinear methods in their respective best areas by imposing a wave-by-wave step function γ_s as a function of cross-shore distance, with $\gamma_s = 0$ prior to breaking and $\gamma_s = 0.42$ post-breaking. The location of the breakpoint for each accepted wave track is determined heuristically (example given in Appendix B). The step function $\gamma_s = (0, 0.42)$ is imposed only at x-locations with at least 10% of the maximum number of phase speed estimates at any x-location during that hover (with the minimum number of estimates included typically between 5 and 11). The average of the individual $\gamma_s = (0, 0.42)$ step functions yields an effective $\gamma(x)$ (Figure 3 e,f green line) that is used to define the “bad” (interpolated over) region for cBathy (Section 4.1). The transition from nonbreaking (here linear) to breaking, nonlinear domains through shoaling in the physical world is captured by the effective $\gamma(x)$ changing gradually from 0 to 0.42.

For each wave track, we invert for depth following linear shallow water theory $h = c^2/g$ ('Linear', Figure 3), or with the nonlinear estimation (Eq. 3, with $\gamma = 0.42$ for 'Nonlinear', and γ_s for 'BP' in Figure 3). The average depth is then computed from the individual tracks with a 5-m Gaussian smoothing applied. Following cBathy methodology, depths are then converted to an elevation (in NAVD88 datum) with a tidal offset, using the average water level over

Composites	cBathy (hErr < 0.5m)	cBathy (breaking parameter)	cBathy (nonlinear)	cBathyCT
$\langle \text{RMSE} \rangle$ (m)				
Surf zone	0.81	0.55	0.44	0.17
Offshore	0.90	0.90	0.92	0.87
Full profile	0.9	0.79	0.76	0.68
$\langle \text{Bias} \rangle$ (m)				
Surf zone	-0.56	-0.41	-0.29	0.06
Offshore	0.58	0.58	0.61	0.58
Full profile	0.12	0.19	0.25	0.38

Table 3

RMSE and Bias statistics for composite models (depth < 10m) at Torrey Pines. surf zone goes from the beginning of wave breaking to the SWL line. Offshore goes from the beginning of wave breaking to 500m offshore.

215 each UAV hover at the nearby La Jolla tide gauge (NOAA station 9410230).

216 4.4. Generating Composite Profiles

217 Profiles spanning from the shoreline to 10-m depth (“composites”) are constructed by combining improved surf
 218 zone bathymetry estimates with cBathy offshore estimates (Figure 5 d,h). The beginning of wave breaking (timestack
 219 derived, Appendix B) is used as the switching location between BP and cBathy estimates. Timestacks are used both to
 220 estimate surf zone depths and to define the shoreward limit of cBathy applicability, where cBathy and crest-tracking
 221 are joined. Example depth estimates have (Figure 5 a-d) varying tidal level and approximately constant wave height
 222 and (Figure 5 e-h) varying wave height and approximately the same tide level. The large surf zone depth errors
 223 ($\langle \text{RMSE} \rangle = 1.42\text{m}$, Figure 5 a,e, Table 3) in raw, unfiltered cBathy are reduced by interpolating across the span
 224 identified as incorrect with timestacks (Figure 5 b,f). Errors in the surf zone are further significantly reduced using the
 225 phase speeds of individual crests and applying a depth inversion individually before smoothing (Gaussian-weighted
 226 5-m moving average) and averaging (Figure 5 c,g).

227 A subaerial beach profile obtained from a low tide RTK-GNSS survey is combined with the subaqueous bathymetry
 228 to obtain a full profile (Figure 5 d,h). When both the survey and bathymetric estimations are available in the same
 229 cross-shore location, the low-tide survey is preferentially selected. By overriding the inner surf zone/swash zone
 230 bathymetry results with a ground-truth survey, we avoid potential issues with wave setup or large depth over-estimations
 231 near the shoreline (Sénéchal et al., 2004; Power et al., 2010; Fiedler et al., 2021). If no overlapping region between
 232 survey and bathymetry estimates exists, the distance between the two are linearly interpolated. The composite profile
 233 has smaller errors ($\langle \text{RMSE} \rangle$ and $\langle \text{Bias} \rangle$) in < 3m depth than either cBathy version. Composite profile normalized
 234 errors ($\langle \text{RMSE} \rangle/h$) vary between 0.1 – 0.2, with largest values near the shoreline (Figure 6). RMSE values offshore
 235 of the surf zone are similar because all methods use cBathy. The mean RMSE varied between 0.05 – 1.75m depending
 236 on conditions (including UAV height, lighting, Hs and other factors). Although using $\gamma(x)$ to determine the bounds of
 237 the surf zone for interpolation within cBathy (rather than hErr) improves the estimates, only breakpoint crest-tracking
 238 accurately captures the terrace in a single hover.

239 5. Discussion

240 5.1. Error sources

241 Holman et al. (2013) proposed mitigating the surf zone gap in cBathy by Kalman filtering cBathy estimations
 242 together, based on hErr, over a tidal cycle. However, tidal variation from $-0.27 - 1.13$ NAVD88m did not shift the
 243 surf zone gap location sufficiently to span the full profile (Figure 5 e). Rather than simply a shoreward shift of a constant
 244 width surf zone as on a plane beach, the observed surf zone both widened and shifted onshore. The location where
 245 cBathy estimates fail changes with tidal elevation (Figure 7) but not enough to generate a full accurate bathymetry
 246 from cBathy alone. Composite profiles are relatively insensitive to tide level (Figure 5 d).

247 The largest (un-normalized) $\langle \text{RMSE} \rangle$ and $\langle \text{Bias} \rangle$ are in the deepest water $h = 8 - 10\text{m}$ (Figure 6, Table 3) where
 248 historical ground-truth (not shown) depths change relatively little ($\langle \text{RMSE} \rangle \sim 0.5\text{m}$). Offshore errors could be reduced
 249 using historical insitu profiles to constrain the range of plausible offshore depths. The extent to which previous ground
 250 truth profiles improve remote estimates (e.g. Kalman filtering) depends on both the characteristics of the available

insitu bathymetry and the beach variability. Kalman filtering is most effective for a beach that is known (from past, extensive, accurate surveys) to change little, or to change predictably in response to changing wave conditions.

UAV rectification uses ground (stability) control points that are limited to the bottom of the field of view, approximately in a straight line, and rarely near the image offshore edge. The resulting roll and pitch errors are corrected with a cross-shore shift (mean shift = 5.4m) when combining remotely-sensed subaqueous and observed subaerial surveys. Including horizon tracking to the least-squares fitting of the camera extrinsics might reduce these offsets and errors in the deepest water (Bergsma et al., 2019; Tsukada et al., 2020).

Normal incidence is not assumed in cBathy, but is assumed with surf zone crest-tracking using timestacks. Waves in the present dataset are primarily normally incident with the largest 10m-depth wave obliquity at Torrey Pines at 12° (Table 1). Assuming Snell's Law, and using 5m as a maximum surf zone depth, errors from neglecting wave obliquity are usually less than 2%. Larger wave obliquities may lead to more obvious overestimation of phase speeds and depth, however, the current dataset limits testing the crest-tracking (CT) part of cBathyCT for obliquely incident waves. Similarly, seas with very broad spectra and therefore many different celerities present in a single timestack may lead to bad estimates with the present surf zone correction. cBathy Phase 1 frequency-wavenumber pairs can be used to determine the appropriateness of a narrow spectrum assumption, by identifying the frequency spread of the 4 most coherent frequencies. Further testing of the method in a larger variety of wave conditions is required to determine the limits of both the normal incidence and narrow spectrum assumptions.

The shallow water approximation for c used in crest-tracking is valid in the present depths (< 5m) with long-period swell ($T_p > 9$ sec) but finite depth theory could readily be used. The peak period as determined from the timestack and a nearby buoy in 17m depth (NOAA NDBC Station 46266) usually differs by less than 1 sec. Outliers in single hovers are removed by using the median of 3 flights rather than a single flight (Figure 8), but overall statistics do not consistently improve. Full profile single-hover profile bias is low owing to cancelling errors ($\langle \text{RMSE} \rangle$ is high) (Table 3).

5.2. Applicability to other sites

Pre-training a U-Net network on a large surf zone dataset provides the network with a good general feature representation. Additional training would be needed for sites with much different incident waves or breaking wave characteristics. A strength of the present methodology is that deep learning is only used as an annotation tool, automating the extraction of crest speeds from timestack-image wave detection, while allowing for depth estimates from different wave dispersion models (here Eq. 1 - 3).

The crest-tracking BP method performs similarly (to Torrey Pines) on the terraced profile at SIO (Figure 2), with mean $\langle \text{RMSE} \rangle = 0.08$ m and $\langle \text{Bias} \rangle = -0.02$ m in the surf zone. Performance was also good at Cardiff on MOP 668, 669, but was degraded by a bedrock reef at the southern edge of the field of view (MOP 667, Figure 9 a). The wave detection algorithm annotates the images accurately (Figure 9 b), but the estimation and inversion from c to depth is inadequate. Nonlinear frequency doubling (e.g. Elgar et al., 1997) on the flat terrace (between $x = 120$ and 200m, Figure 9 a) may create additional crests that would confound simple crest-conserving inversions.

The effect of alongshore variations in bathymetry on phase speed and crest direction is neglected here, but could be included in more sophisticated 2D inversions both within and seaward of the surf zone.

The $\gamma = 0.42$ used here is based on historical observations at Torrey Pines (Thornton and Guza, 1982). LiDAR wavescans concurrent with UAV hovers yield a local $\gamma(x)$ (Figure 10), computed from direct sea surface elevation measurements (H_{m_0}) and insitu surveys (Fiedler et al., 2021). The average γ over the surf zone varies between 0.55 – 0.74, decreasing offshore. Deviations in gamma estimations at these sites do not significantly affect the bathymetric estimations; mean $\langle \text{RMSE} \rangle = 0.25$ m is minimum over all available transects for $0.4 < \gamma < 0.5$, increasing only slightly to 0.3m for $0.6 < \gamma < 0.8$. Yoo et al. (2011) reported $\gamma = 0.6$ in their crest-tracking study. Note in 'low' wave conditions ($H_s < 0.75$ m), linear crest-tracking ($\gamma = 0$) and BP perform comparably well with $\langle \text{RMSE} \rangle \sim 0.18$ m in the breaking region. Not surprisingly, corrections for wave nonlinearity are most important when H_s is largest. The present approach ($\gamma = 0.42$) likely fails in shallow water on steep slopes where plunging waves with $\gamma > 0.8$ are expected. Concurrent video and LiDAR (e.g. Figure 10) of γ and c would enable application of the present method to sites with much different breaking wave characteristics and γ .

Results for individual 17 min hovers are encouraging. The dependence of cBathy and crest-tracking error statistics (e.g. $\langle \text{RMSE} \rangle$) on record length is unknown, and likely varies with wave conditions and bathymetry. Errors in composite profiles do not depend significantly on tide level for the present limited range of conditions but may depend on tide level on barred bathymetry. Additional model testing and calibration is needed.

303 **A. Wave-crest Detection Deep Learning Algorithm**

304 The U-Net architecture (Ronneberger et al., 2015) is well established for segmentation tasks such as crest detection.
 305 U-Nets are based on an Encoder-Decoder architecture, with skip connections from the Encoder to the Decoder at
 306 the different levels to be able to recover resolution. The Encoder provides a compact feature representation (many
 307 features, but little resolution) of the input image by applying convolutions followed by a maxpool downsampling at
 308 multiple levels (more features, less resolution). The Decoder takes the compact feature representation and provides a
 309 classification for each pixel in the image at full resolution by upsampling followed by concatenation and convolutions
 310 at multiple levels (fewer features, more resolution). We used a modified version of the U-Net with a ResNet18 encoder
 311 pre-trained on the ImageNet dataset (Usuyama, 2018) (Figure 4).

312 Wave crest detection uses a limited neighborhood area in timestamp-images. Training and prediction can use small
 313 high-resolution image tiles, increasing the training dataset size and reducing the deep learning network complexity. To
 314 augment the training dataset, image tiles are sampled at arbitrary locations in the image. Timestamp-images are 5000
 315 pixels cross-shore direction and a time-dependent width of 600 pixels per minute. For the training, we sample 1000
 316 256 x 256 image tiles from a timestamp-image. For the prediction, we divide the timestamp-image into overlapping 256
 317 x 256 image tiles. The border of the predicted image tiles (therefore the overlap) has relatively large errors and is not
 318 used. Thresholds such as minimum length and width of detected track can be specified.

319 A binary cross-entropy (BCE) loss function is used for binary classification (limited to a region around the sparse
 320 ground-truth), with a Root-Mean-Square (RMS) optimizer and an adaptive learning rate scheduler. The model is
 321 trained for 50 epochs, with a batch size of 8 and an initial adaptive learning rate of 0.0001. Training and validation
 322 losses remained constant after 40 epochs. Model predictions are made after 50 epochs. The deep learning approach
 323 was implemented in Python and PyTorch. A desktop computer with a GeForce GTX 1660 GPU required 50 hours to
 324 train the model for 50 epochs, with predictions taking 2.5 min per timestamp.

325 **B. Breakpoint locator**

326 The breakpoint location is determined with an algorithm based on pixel intensity gradients along a wave track.
 327 Thresholds for broken and unbroken waves are determined by fitting two Gaussian distributions to the image pixel
 328 intensity histograms (Figure 11 a) and determining the mean of the distributions. Individual waves track may include
 329 only broken or only unbroken waves, with relatively small gradients, and high or low pixel intensity levels (red and
 330 black circles respectively, Figure 11 a). Tracks that include the breakpoint begin unbroken (below the low threshold),
 331 with a sharp gradient (purple dot, Figure 11 c) when breaking begins, and a high but stable pixel intensity above the
 332 high threshold (green circle, Figure 11 b). The breakpoint location is set to the location of maximum gradient. Residual
 333 foam can obscure sharp breakpoint gradients, and each wave track goes through an iterative process to determine if
 334 it contains the breakpoint. Failing a conclusive result with the first pass with the strictest thresholds, less stringent
 335 thresholds are applied until the segment is characterized (examples provided in the attached code). The breaking
 336 location estimated by the algorithm and visual inspection agree.

337 **Acknowledgments**

338 This study was funded by the U.S. Army Corps of Engineers (W912HZ1920020) and the California Department
 339 of Parks and Recreation (C19E0026). Data were collected and processed by the Coastal Processes Group field team
 340 members Lucian Parry, Rob Grenzeback, Kent Smith, Brian Woodward, Greg Boyd, and Mele Johnson. Michele
 341 Okihiro organized logistics.

342 **CRediT authorship contribution statement**

343 **Athina M.Z. Lange:** Conceptualization, Investigation, Formal analysis, Writing - Original Draft, Visualization.
 344 **Julia W. Fiedler:** Conceptualization, Methodology, Writing - Review & Editing. **Mark A. Merrifield:** Conceptu-
 345 alization, Writing - Review & Editing, Funding acquisition. **R. T. Guza:** Conceptualization, Writing - Review &
 346 Editing.

347 **References**

- 348 Aarninkhof, S.G.J., 2005. Nearshore subtidal bathymetry from time-exposure video images. *Journal of Geophysical Research* 110, C06011. URL:
 349 <http://doi.wiley.com/10.1029/2004JC002791>, doi:10.1029/2004JC002791.
- 350 Abileah, R., Trizna, D.B., 2010. Shallow water bathymetry with an incoherent X-band radar using small (smaller) space-time image cubes, in: 2010
 351 IEEE International Geoscience and Remote Sensing Symposium, IEEE, Honolulu, HI, USA. pp. 4330–4333. URL: <http://ieeexplore.ieee.org/document/5654386/>, doi:10.1109/IGARSS.2010.5654386.
- 352 Almar, R., Bonneton, P., Sénéchal, N., Roelvink, D., 2009. WAVE CELERITY FROM VIDEO IMAGING: A NEW METHOD, in: Coastal
 353 Engineering 2008, World Scientific Publishing Company, Hamburg, Germany. pp. 661–673. URL: http://www.worldscientific.com/doi/abs/10.1142/9789814277426_0056, doi:10.1142/9789814277426_0056.
- 354 Basco, D.R., 1985. A Qualitative Description of Wave Breaking. *Journal of Waterway, Port, Coastal, and Ocean Engineering* 111, 171–188.
- 355 Bergsma, E., Conley, D., Davidson, M., O'Hare, T., 2016. Video-based nearshore bathymetry estimation in macro-tidal environments. *Marine Geology* 374, 31–41. URL: <https://linkinghub.elsevier.com/retrieve/pii/S0025322716300159>, doi:10.1016/j.margeo.2016.02.001.
- 356 Bergsma, E.W., Almar, R., Melo de Almeida, L.P., Sall, M., 2019. On the operational use of UAVs for video-derived bathymetry. *Coastal Engineering* 152, 103527. URL: <https://linkinghub.elsevier.com/retrieve/pii/S0378383918303582>, doi:10.1016/j.coastaleng.2019.103527.
- 357 Brodie, K.L., Bruder, B.L., Slocum, R.K., Spore, N.J., 2019. Simultaneous Mapping of Coastal Topography and Bathymetry From a Lightweight
 358 Multicamera UAS. *IEEE Transactions on Geoscience and Remote Sensing* 57, 6844–6864. URL: <https://ieeexplore.ieee.org/document/8726410/>, doi:10.1109/TGRS.2019.2909026.
- 359 Brodie, K.L., Palmsten, M.L., Hesser, T.J., Dickhut, P.J., Raubenheimer, B., Ladner, H., Elgar, S., 2018. Evaluation of video-based linear depth in-
 360 version performance and applications using altimeters and hydrographic surveys in a wide range of environmental conditions. *Coastal Engineering* 136, 147–160. URL: <https://linkinghub.elsevier.com/retrieve/pii/S0378383917301989>, doi:10.1016/j.coastaleng.2018.01.003.
- 361 Bruder, B.L., Brodie, K.L., 2020. CIRN Quantitative Coastal Imaging Toolbox. *SoftwareX* 12, 100582. URL: <https://linkinghub.elsevier.com/retrieve/pii/S2352711020302958>, doi:10.1016/j.softx.2020.100582.
- 362 Catálan, P.A., Haller, M.C., 2008. Remote sensing of breaking wave phase speeds with application to non-linear depth inversions. *Coastal Engineering* 55, 93–111. URL: <https://linkinghub.elsevier.com/retrieve/pii/S0378383907001007>, doi:10.1016/j.coastaleng.2007.09.010.
- 363 Collins, A., Brodie, K., Bak, A.S., Hesser, T., Farthing, M., Lee, J., Long, J., 2020. Bathymetric Inversion and Uncertainty Estimation from
 364 Synthetic Surf-Zone Imagery with Machine Learning. *Remote Sensing* 12, 3364. URL: <https://www.mdpi.com/2072-4292/12/20/3364>, doi:10.3390/rs12203364.
- 365 van Dongeren, A., Plant, N., Cohen, A., Roelvink, D., Haller, M.C., Catalán, P., 2008. Beach Wizard: Nearshore bathymetry estimation through
 366 assimilation of model computations and remote observations. *Coastal Engineering* 55, 1016–1027. URL: <https://linkinghub.elsevier.com/retrieve/pii/S0378383908000884>, doi:10.1016/j.coastaleng.2008.04.011.
- 367 Elgar, S., Guza, R.T., Raubenheimer, B., Herbers, T.H.C., Gallagher, E.L., 1997. Spectral evolution of shoaling and breaking waves on a barred
 368 beach. *Journal of Geophysical Research: Oceans* 102, 15797–15805. URL: <http://doi.wiley.com/10.1029/97JC01010>, doi:10.1029/97JC01010.
- 369 Fiedler, J.W., Kim, L., Grenzeback, R., Young, A., Merrifield, M.A., 2021. Enhanced Surf Zone and Wave Runup Observations with Hovering
 370 Drone-Mounted Lidar. *Journal of Atmospheric and Oceanic Technology* 38, 1967–1978. URL: <https://journals.ametsoc.org/view/journals/atot/38/11/JTECH-D-21-0027.1.xml>, doi:10.1175/JTECH-D-21-0027.1.
- 371 Gao, J., 2009. Bathymetric mapping by means of remote sensing: methods, accuracy and limitations. *Progress in Physical Geography: Earth and Environment* 33, 103–116. URL: <http://journals.sagepub.com/doi/10.1177/0309133309105657>, doi:10.1177/0309133309105657.
- 372 Geyman, E.C., Maloof, A.C., 2019. A Simple Method for Extracting Water Depth From Multispectral Satellite Imagery in Regions of Variable
 373 Bottom Type. *Earth and Space Science* 6, 527–537. URL: <https://onlinelibrary.wiley.com/doi/abs/10.1029/2018EA000539>, doi:10.1029/2018EA000539.
- 374 Holland, T., 2001. Application of the linear dispersion relation with respect to depth inversion and remotely sensed imagery. *IEEE Transactions on
 375 Geoscience and Remote Sensing* 39, 2060–2072. URL: <http://ieeexplore.ieee.org/document/951097/>, doi:10.1109/36.951097.
- 376 Holman, R., Bergsma, E.W.J., 2021. Updates to and Performance of the cBathy Algorithm for Estimating Nearshore Bathymetry from Remote
 377 Sensing Imagery. *Remote Sensing* 13, 3996. URL: <https://www.mdpi.com/2072-4292/13/19/3996>, doi:10.3390/rs13193996.
- 378 Holman, R., Haller, M.C., 2013. Remote Sensing of the Nearshore. *Annual Review of Marine Science* 5, 95–113. URL: <http://www.annualreviews.org/doi/10.1146/annurev-marine-121211-172408>, doi:10.1146/annurev-marine-121211-172408.
- 379 Holman, R., Plant, N., Holland, T., 2013. cBathy: A robust algorithm for estimating nearshore bathymetry: The cBathy Algorithm. *Journal of
 380 Geophysical Research: Oceans* 118, 2595–2609. URL: <http://doi.wiley.com/10.1002/jgrc.20199>, doi:10.1002/jgrc.20199.
- 381 Holman, R., Stanley, J., 2007. The history and technical capabilities of Argus. *Coastal Engineering* 54, 477–491. URL: <https://linkinghub.elsevier.com/retrieve/pii/S037838390700018X>, doi:10.1016/j.coastaleng.2007.01.003.
- 382 Inman, D.L., Tait, R.J., Nordstrom, C.E., 1971. Mixing in the surf zone. *Journal of Geophysical Research* 76, 3493–3514. URL: <http://doi.wiley.com/10.1029/JC076i015p03493>, doi:10.1029/JC076i015p03493.
- 383 Jing, E., Datt, B., 2010. Detection of coastal bathymetry using hyperspectral imagery, in: OCEANS'10 IEEE SYDNEY, IEEE, Sydney, Australia.
 384 pp. 1–4. URL: <http://ieeexplore.ieee.org/document/5603864/>, doi:10.1109/OCEANSSYD.2010.5603864.
- 385 Jordi, A., Georgas, N., Blumberg, A., Yin, L., Chen, Z., Wang, Y., Schulte, J., Ramaswamy, V., Runnels, D., Saleh, F., 2019. A Next-Generation
 386 Coastal Ocean Operational System: Probabilistic Flood Forecasting at Street Scale. *Bulletin of the American Meteorological Society* 100, 41–54.
 387 URL: <https://journals.ametsoc.org/view/journals/bams/100/1/bams-d-17-0309.1.xml>, doi:10.1175/BAMS-D-17-0309.1.
- 388 Legleiter, C.J., Harrison, L.R., 2019. Remote Sensing of River Bathymetry: Evaluating a Range of Sensors, Platforms, and Algorithms on the

- 410 Upper Sacramento River, California, USA. *Water Resources Research* 55, 2142–2169. URL: <https://onlinelibrary.wiley.com/doi/abs/10.1029/2018WR023586>, doi:10.1029/2018WR023586.
- 411 Li, J., Knapp, D.E., Schill, S.R., Roelfsema, C., Phinn, S., Silman, M., Mascaro, J., Asner, G.P., 2019. Adaptive bathymetry estimation for shallow
412 coastal waters using Planet Dove satellites. *Remote Sensing of Environment* 232, 111302. URL: <https://linkinghub.elsevier.com/retrieve/pii/S0034425719303219>, doi:10.1016/j.rse.2019.111302.
- 413 Lippmann, T.C., Holman, R., 1991. Phase Speed and Angle of Breaking Waves Measured with Video Techniques, pp. 542–556.
- 414 Lippmann, T.C., Holman, R.A., 1989. Quantification of sand bar morphology: A video technique based on wave dissipation. *Journal of Geophysical
415 Research* 94, 17.
- 416 Mallet, C., Bretar, F., 2009. Full-waveform topographic lidar: State-of-the-art. *ISPRS Journal of Photogrammetry and Remote Sensing* 64, 1–16.
417 URL: <https://linkinghub.elsevier.com/retrieve/pii/S0924271608000993>, doi:10.1016/j.isprsjprs.2008.09.007.
- 418 Martins, K., Blenkinsopp, C.E., Deigaard, R., Power, H.E., 2018. Energy Dissipation in the Inner Surf Zone: New Insights From Li <span
419 style="font-variant:small-caps;">DAR-Based Roller Geometry Measurements. *Journal of Geophysical Research: Oceans* 123,
420 3386–3407. URL: <https://onlinelibrary.wiley.com/doi/abs/10.1029/2017JC013369>, doi:10.1029/2017JC013369.
- 421 Merrifield, M.A., Johnson, M., Guza, R.T., Fiedler, J.W., Young, A.P., Henderson, C., Lange, A.M., O'Reilly, W.C., Ludka, B.C., Okihiro, M.,
422 Pappas, K., Engeman, L., Behrens, J., Terrill, E., 2021. An early warning system for wave-driven coastal flooding at Imperial Beach, CA.
423 *Natural Hazards*.
- 424 O'Reilly, W., Olfe, C.B., Thomas, J., Seymour, R., Guza, R., 2016. The California coastal wave monitoring and prediction system. *Coastal Engineering* 116, 118–132. URL: <https://linkinghub.elsevier.com/retrieve/pii/S0378383916301120>, doi:10.1016/j.coastaleng.2016.06.005.
- 425 Plant, N.G., Edwards, K.L., Kaihatu, J.M., Veeramony, J., Hsu, L., Holland, K.T., 2009. The effect of bathymetric filtering on nearshore process model results. *Coastal Engineering* 56, 484–493. URL: <https://linkinghub.elsevier.com/retrieve/pii/S0378383908001841>, doi:10.1016/j.coastaleng.2008.10.010.
- 426 Power, H.E., Hughes, M.G., Aagaard, T., Baldoock, T.E., 2010. Nearshore wave height variation in unsaturated surf. *Journal of Geophysical Research* 115, C08030. URL: <http://doi.wiley.com/10.1029/2009JC005758>, doi:10.1029/2009JC005758.
- 427 Radermacher, M., Wengrove, M., van Thiel de Vries, J., Holman, R., 2014. Applicability of video-derived bathymetry estimates to nearshore current
428 model predictions. *Journal of Coastal Research* 70, 290–295. URL: <http://www.bioone.org/doi/10.2112/SI70-049.1>, doi:10.2112/SI70-049.1.
- 429 Raubenheimer, B., Guza, R.T., Elgar, S., 1996. Wave transformation across the inner surf zone. *Journal of Geophysical Research: Oceans* 101,
430 25589–25597. URL: <http://doi.wiley.com/10.1029/96JC02433>, doi:10.1029/96JC02433.
- 431 Rodríguez-Padilla, I., Castelle, B., Marieu, V., Morichon, D., 2022. Video-Based Nearshore Bathymetric Inversion on a Geologically Constrained
432 Mesotidal Beach during Storm Events. *Remote Sensing* 14, 3850. URL: <https://www.mdpi.com/2072-4292/14/16/3850>, doi:10.3390/rs14163850.
- 433 Ronneberger, O., Fischer, P., Brox, T., 2015. U-Net: Convolutional Networks for Biomedical Image Segmentation. arXiv:1505.04597 [cs] URL:
434 <http://arxiv.org/abs/1505.04597>. arXiv: 1505.04597.
- 435 Rutten, J., de Jong, S.M., Ruessink, G., 2017. Accuracy of Nearshore Bathymetry Inverted From \${X}\$ -Band Radar and Optical Video Data. *IEEE
436 Transactions on Geoscience and Remote Sensing* 55, 1106–1116. URL: <http://ieeexplore.ieee.org/document/7738400/>, doi:10.
437 1109/TGRS.2016.2619481.
- 438 Gomes da Silva, P., Coco, G., Garnier, R., Klein, A.H., 2020. On the prediction of runup, setup and swash on beaches. *Earth-Science Reviews*
439 204, 103148. URL: <https://linkinghub.elsevier.com/retrieve/pii/S0012825219306828>, doi:10.1016/j.earscirev.2020.
440 103148.
- 441 Stephens, E., Cloke, H., 2014. Improving flood forecasts for better flood preparedness in the UK (and beyond): Commentary. *The Geographical
442 Journal* 180, 310–316. URL: <http://doi.wiley.com/10.1111/geoj.12103>, doi:10.1111/geoj.12103.
- 443 Stive, M.J.F., 1980. VELOCITY AND PRESSURE FIELD OF SPILLING BREAKERS. *COASTAL ENGINEERING*, 20.
- 444 Stockdon, H.F., Holman, R.A., 2000. Estimation of wave phase speed and nearshore bathymetry from video imagery. *Journal of Geophysical
445 Research: Oceans* 105, 22015–22033. URL: <http://doi.wiley.com/10.1029/1999JC000124>, doi:10.1029/1999JC000124.
- 446 Stokes, K., Poate, T., Masselink, G., 2019. DEVELOPMENT OF A REAL-TIME, REGIONAL COASTAL FLOOD WARNING SYSTEM FOR
447 SOUTHWEST ENGLAND, in: *Coastal Sediments 2019, WORLD SCIENTIFIC*, Tampa/St. Petersburg, Florida, USA. pp. 1460–1474. URL:
448 https://www.worldscientific.com/doi/abs/10.1142/9789811204487_0127, doi:10.1142/9789811204487_0127.
- 449 Stokes, K., Poate, T., Masselink, G., King, E., Saulter, A., Ely, N., 2021. Forecasting coastal overtopping at engineered and naturally defended
450 coastlines. *Coastal Engineering* 164, 103827. URL: <https://linkinghub.elsevier.com/retrieve/pii/S0378383920305135>, doi:10.
451 1016/j.coastaleng.2020.103827.
- 452 Stringari, C., Harris, D., Power, H., 2019. A novel machine learning algorithm for tracking remotely sensed waves in the surf zone. *Coastal Engineering* 147,
453 149–158. URL: <https://linkinghub.elsevier.com/retrieve/pii/S037838391830228X>, doi:10.1016/j.coastaleng.
454 2019.02.002.
- 455 Svendsen, I.A., Buhr Hansen, J., 1976. Deformation up to Breaking of Periodic Waves on a Beach, in: *Proceedings, 15th International Conference
456 on Coastal Engineering*, pp. 520–539.
- 457 Svendsen, I.A., Qin, W., Ebersole, B.A., 2003. Modelling waves and currents at the LSTF and other laboratory facilities. *Coastal Engineering* 50,
458 19–45. URL: <https://linkinghub.elsevier.com/retrieve/pii/S0378383903000772>, doi:10.1016/S0378-3839(03)00077-2.
- 459 Szeliski, R., 2022. *Computer Vision: Algorithms and Applications*, 2nd Edition. 2 ed., Springer.
- 460 Sénéchal, N., Dupuis, H., Bonneton, P., 2004. Preliminary hydrodynamic results of a field experiment on a barred beach, True Vert beach on October
461 2001. *Ocean Dynamics* 54, 408–414. doi:<https://doi.org/10.1007/s10236-003-0052-9>.
- 462 Thornton, E.B., Guza, R.T., 1982. Energy saturation and phase speeds measured on a natural beach. *Journal of Geophysical Research* 87, 9499.
463 URL: <http://doi.wiley.com/10.1029/JC087iC12p09499>, doi:10.1029/JC087iC12p09499.

- 473 Thuan, D.H., Almar, R., Marchesiello, P., Viet, N.T., 2019. Video Sensing of Nearshore Bathymetry Evolution with Error Estimate. *Journal of*
474 *Marine Science and Engineering* 7, 233. URL: <https://www.mdpi.com/2077-1312/7/7/233>, doi:10.3390/jmse7070233.
- 475 Tissier, M., Bonneton, P., Michallet, H., Ruessink, B.G., 2015. Infragravity-wave modulation of short-wave celerity in the surf zone. *Journal of*
476 *Geophysical Research: Oceans* 120, 6799–6814. URL: <https://onlinelibrary.wiley.com/doi/abs/10.1002/2015JC010708>, doi:10.
477 1002/2015JC010708.
- 478 Tsukada, F., Shimozono, T., Matsuba, Y., 2020. UAV-based mapping of nearshore bathymetry over broad areas. *Coastal Engineering Journal*
479 62, 285–298. URL: [https://www.tandfonline.com/doi/full/10.1080/21664250.2020.
480 1747766](https://www.tandfonline.com/doi/full/10.1080/21664250.2020.1747766).
- 481 USGS, 2022. Total Water Level and Coastal Change Forecast Viewer. URL: [https://coastal.er.usgs.gov/hurricanes/research/
482 twlviewer/](https://coastal.er.usgs.gov/hurricanes/research/twlviewer/).
- 483 Usuyama, N., 2018. Simple PyTorch implementations of U-Net/FullyConvNet (FCN) for image segmentation. URL: [https://github.com/
484 usuyama/pytorch-unet](https://github.com/usuyama/pytorch-unet).
- 485 Vanderstraete, T., Goossens, R., Ghabour, T., 2003. Remote sensing as a tool for bathymetric mapping of coral reefs in the Red Sea (Hurghada –
486 Egypt). *Belgeo* , 257–268URL: <http://journals.openedition.org/belgeo/16652>, doi:10.4000/belgeo.16652.
- 487 Wengrove, M.E., Henriquez, M., de Schipper, M.A., Holman, R., Stive, M.J.F., 2013. MONITORING MORPHOLOGY OF THE SAND ENGINE
488 LEESIDE USING ARGUS' cBATHY. *Coastal Dynamics* , 13.
- 489 Yoo, J., Fritz, H.M., Haas, K.A., Work, P.A., Barnes, C.F., 2011. Depth Inversion in the Surf Zone with Inclusion of Wave Nonlinearity Using
490 Video-Derived Celerity. *Journal of Waterway, Port, Coastal, and Ocean Engineering* 137, 95–106. URL: [http://ascelibrary.org/doi/10.1061/\(ASCE\)WW.1943-5460.0000068](http://ascelibrary.org/doi/10.1061/(ASCE)WW.1943-5460.0000068), doi:10.1061/(ASCE)WW.1943-5460.0000068.
- 491 Zuckerman, S., Anderson, S., 2018. Bathymetry and Water-Level Estimation Using X-Band Radar at a Tidal Inlet. *Journal of Coastal Research* 345,
492 1227–1235. URL: <http://www.bioone.org/doi/10.2112/JCOASTRES-D-17-00182.1>, doi:10.2112/JCOASTRES-D-17-00182.1.
- 493

494 List of Figures

- 542 8 Histograms of depth inversion errors at Torrey Pines (for the surf zone region) for different methods 21
 543 (stacked vertically) on 59 transects (left) 1 hover and (right) median of 3 hovers. (a,b) cBathy with
 544 interpolation where $hErr < 0.5m$, (c,d) cBathy with breaking criterion for surf zone interpolation
 545 and nonlinear gamma correction, and (e,f) composite using breakpoint crest-tracking cBathyCT, (g,h)
 546 mean bias of cBathyCT. Colored by offshore H_s (legend). Outliers with the largest bias and RMSE are
 547 removed with 3 hovers. Fit statistics in Table 3. Probabilities (vertical axis) sum to 1.0.
 548 9 (left) Depth versus cross-shore distance from 1 hover on MOP 667 - 669 (stacked with a 5m vertical
 549 offset). Ground truth (black), cBathy with $hErr < 0.5m$ (red), cBathy with a nonlinear correction
 550 (blue) and cBathyCT (green). Bedrock reef on MOP 667 from $x = 125m$ to 1km offshore. (right)
 551 Results of the deep-learning crest-tracking algorithm on MOP 667. The wave crest detection neural
 552 network was not trained on reef-like profiles, but may detect wave crests accurately enough for use in
 553 alternative (e.g. 2D nonlinear) depth inversions. 22
 554 10 (left) for 468 transects, median RMSE versus γ (green curve), (boxes) 50% quantile, (black bars) 90%
 555 quantile for crest-tracking BP method in the surf zone (outliers red dots). Minimum $\langle RMSE \rangle$ at
 556 $\gamma = 0.4$ increases $< 20\%$ for $0.1 < \gamma < 0.7$. (right) surf zone LiDAR measured $\gamma = H_{m_0}/h$ versus
 557 cross-shore distance for (b) Nov 2nd, 2021, $H_s = 1.12m$, (c) Oct 26th, 2021, $H_s = 1.92m$, (d) Dec
 558 15th, 2021, $H_s = 2.15m$, colored by hover. Black horizontal line is mean γ over surf zone. 23
 559 11 Schematic of breakpoint location using gradients of pixel intensity. (left) histogram of pixel intensity
 560 of the full image (10^7 counts are shown) typically have two maxima and each is fit to a Gaussian
 561 distribution, centered around high and low thresholds (red and yellow respectively). (middle) idealized
 562 pixel intensity versus location on wave track segment completely within (all broken) or completely
 563 seaward (unbroken) of surf zone (red and black circles, respectively). Sharp gradients (green) indicate
 564 breakpoint. (right) idealized pixel intensity gradient versus along-track location. 24

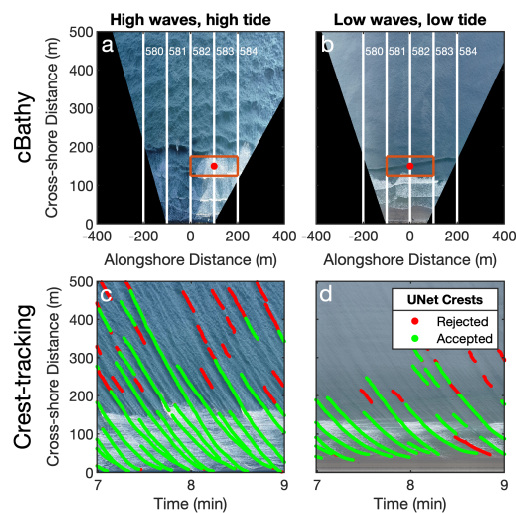


Figure 1: Contrasting conditions (left) Dec 15th, 2021, relatively high waves and high tide ($H_s = 1.96\text{m}$, tide = 1.41m) and (right) Dec 2nd, 2021, lower waves and lower tide ($H_s = 0.64\text{m}$, tide = 0.46m). Beach is at the bottom of each image. (Top) Orthorectified planview images of shoaling region and surf zone. Orange rectangle encloses 200m-alongshore by 50m-cross-shore area used for each cBathy depth estimate (red dot). Box dimensions increase offshore. Ground-truth cross-shore transects (white) are identified by “MOP” number. (Bottom) wave crest trajectories (cross-shore location versus time) determined by a deep learning algorithm on MOPs (c) 583 and (d) 582. Red trajectories were rejected for further analysis.

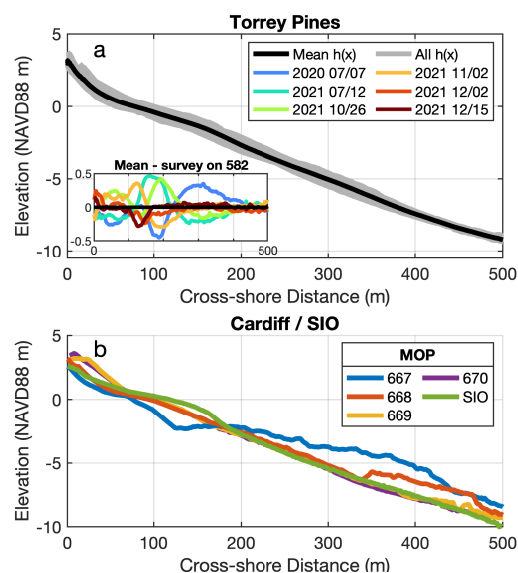


Figure 2: Seabed elevation versus cross-shore distance at (a) Torrey Pines. Mean of all transects and days (bold, $n = 42$) and shaded by range of all observed profiles. (insert) Deviations of MOP 582 transect from mean, colored by date. (b) Cardiff (reef at $x > 125\text{m}$ on MOP 667, blue) and SIO (green MOP 514).

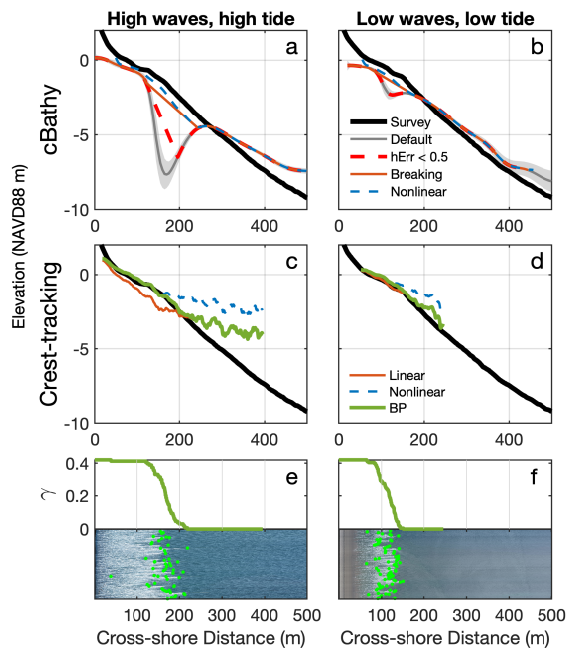


Figure 3: Bed elevation versus cross-shore distance for relatively (a,c) high waves and tide, Dec 15th, 2021 ($H_s = 1.96\text{m}$, tide = 1.41m) and (b,d) low waves and tide, Dec 2nd 2021 ($H_s = 0.64\text{m}$, tide = 0.46m) at Torrey Pines State Beach, USA. Mean ground-truth survey (black). Remote sensing estimates: (a,b) cBathy: default (gray with $h\text{Err}$ shaded), $h\text{Err} > 0.5\text{m}$ removed and interpolated over (red dashed), breaking region removed and interpolated (red solid) and (best cBathy-only method) with a nonlinear correction (blue dashed). (c,d) crest-tracking, linear (solid red), nonlinear (blue dashed), breakpoint transition (green). (e,f) effective $\gamma = H/h$ versus cross-shore distance above compressed view of the corresponding timestamp with detected breakpoints shown (green dots). Effective $\gamma(x)$ is the mean of γ step functions for all waves in a given hover.

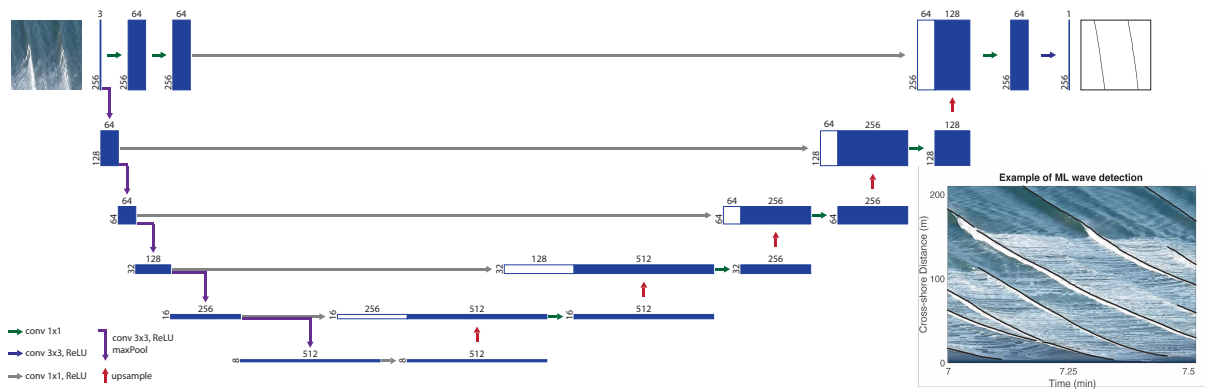


Figure 4: U-Net Architecture: Number of features on top and resolution (number of pixels) to the left of the blocks. (insert) Example of ML wave crest detection.

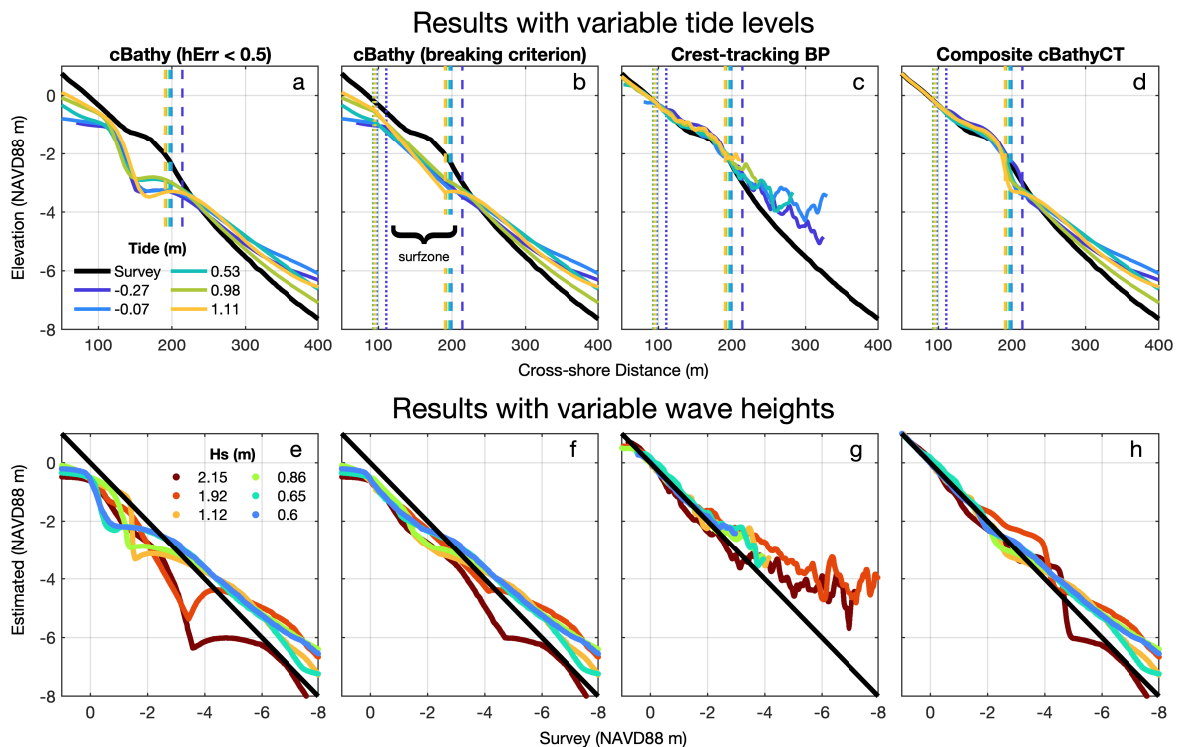


Figure 5: Bathymetry estimates at Torrey Pines MOP 582. Upper panels show July 7th, 2020 elevation versus cross-shore distance for varying tide levels (1.3m max difference, legend). The dotted vertical line (upper panels) marks the shoreward edge of surf zone and offshore extent of subaerial survey where the crest tracking method (c,g) is fused with insitu data for composite cBathyCT (d,h). Vertical dashed lines mark beginning of wave breaking where cBathy (b,f) and crest-tracking bathymetry (c,g) are stitched together to form the composite (d,h). Bottom panels show estimated versus observed elevation for varying wave heights (legend) near mid-tide on various dates (Table 1). Solid black is ground truth. Bathymetry estimates are shown from cBathy interpolated over $h_{Err} < 0.5$ (a,e), cBathy interpolated over the breaking region (b,f), breakpoint transition crest-tracking (c,g) and cBathyCT (d,h). Owing to the non-planar beach profile, the stitching location varied little with tide (top panel, dotted line). Fit statistics for various composites are in Table 3.

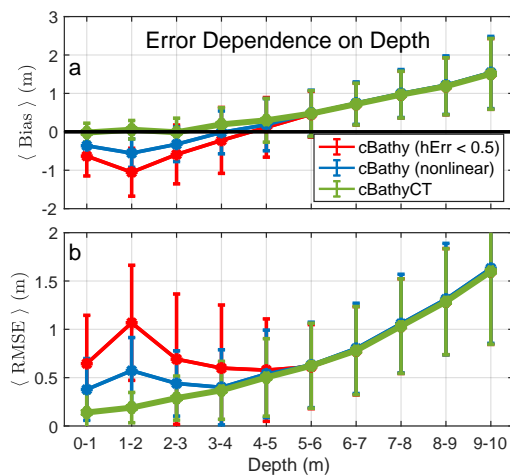


Figure 6: Torrey Pines composite bathymetry mean statistics from 59 full profiles, binned by depth (solid curves). (top) mean Bias, (bottom) mean RMSE. Curve color indicates surf zone method: (red) cBathy estimate with $h\text{Err} < 0.5\text{m}$, (blue) cBathy with breaking criterion for surf zone interpolation and nonlinear gamma correction, (green) cBathy with breakpoint transition crest-tracking in the surf zone (cBathyCT). Seaward of breaking, methods all use cBathy and curves overlap. Depth is relative to the still water line, accounting for tides but not setup. Error bars show standard deviation. For cBathyCT composite, the normalized standard $\langle \text{RMSE} \rangle / h = 0.27, 0.13, 0.11, \text{ and } 0.15$ for bin centered on 0.5, 1.5, 4.5, and 8.5m respectively.

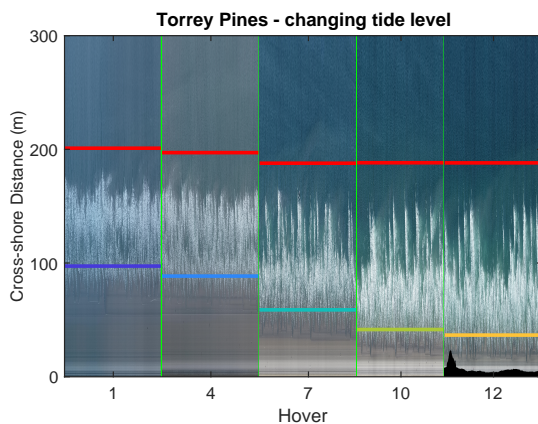


Figure 7: Torrey Pines MOP 582 on July 7th, 2020. Wave height $H_s \sim 0.89\text{m}$. Timestacks (intensity versus time on a cross-shore transect) for 5, 17-min hovers during flood tide, separated by green vertical lines. The waterline (colored horizontal lines, Figure 5 a) gradually moves onshore 60m (from $x = 97\text{m}$ to 37m) during flood (1.37m tide increase). The shoreward limit of accurate cBathy (solid red lines) includes breaking in the 50m-wide sample window. The offshore boundary moves onshore only 12m (from $x = 200\text{m}$ to 188 m) owing to a small terrace (Figure 2) that triggers breaking.

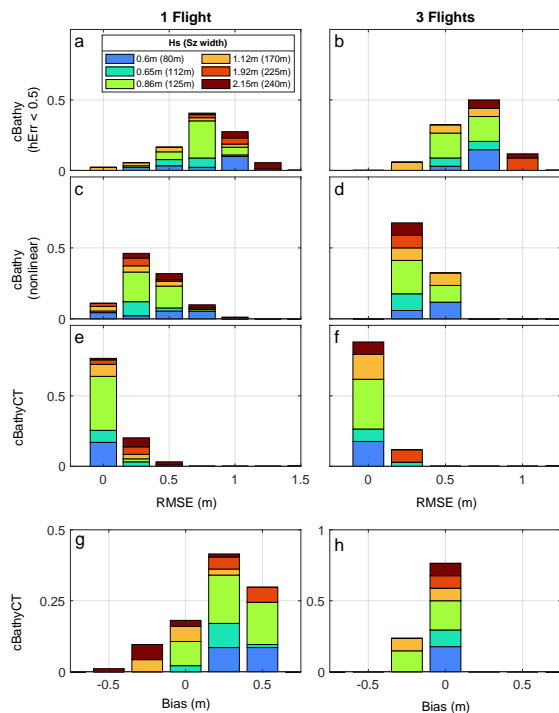


Figure 8: Histograms of depth inversion errors at Torrey Pines (for the surf zone region) for different methods (stacked vertically) on 59 transects (left) 1 hover and (right) median of 3 hovers. (a,b) cBathy with interpolation where $h\text{Err} < 0.5\text{m}$, (c,d) cBathy with breaking criterion for surf zone interpolation and nonlinear gamma correction, and (e,f) composite using breakpoint crest-tracking cBathyCT, (g,h) mean bias of cBathyCT. Colored by offshore Hs (legend). Outliers with the largest bias and RMSE are removed with 3 hovers. Fit statistics in Table 3. Probabilities (vertical axis) sum to 1.0.

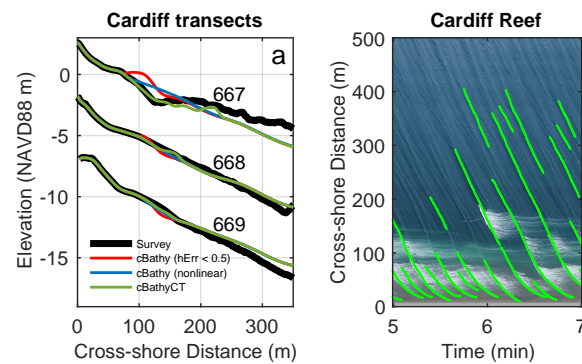


Figure 9: (left) Depth versus cross-shore distance from 1 hover on MOP 667 - 669 (stacked with a 5m vertical offset). Ground truth (black), cBathy with $h\text{Err} < 0.5\text{m}$ (red), cBathy with a nonlinear correction (blue) and cBathyCT (green). Bedrock reef on MOP 667 from $x = 125\text{m}$ to 1km offshore. (right) Results of the deep-learning crest-tracking algorithm on MOP 667. The wave crest detection neural network was not trained on reef-like profiles, but may detect wave crests accurately enough for use in alternative (e.g. 2D nonlinear) depth inversions.

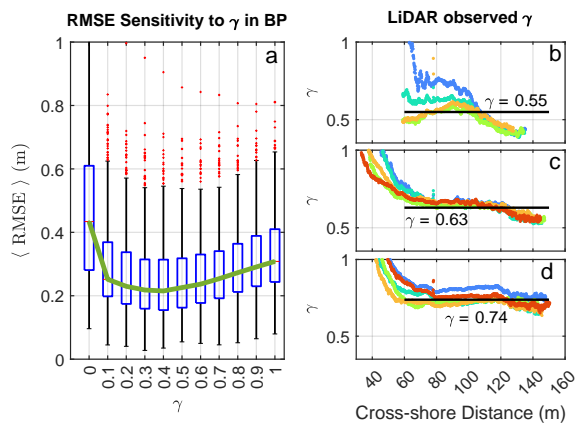


Figure 10: (left) for 468 transects, median RMSE versus γ (green curve), (boxes) 50% quantile, (black bars) 90% quantile for crest-tracking BP method in the surf zone (outliers red dots). Minimum $\langle \text{RMSE} \rangle$ at $\gamma = 0.4$ increases $< 20\%$ for $0.1 < \gamma < 0.7$. (right) surf zone LiDAR measured $\gamma = H_{m_0}/h$ versus cross-shore distance for (b) Nov 2nd, 2021, $H_s = 1.12\text{m}$, (c) Oct 26th, 2021, $H_s = 1.92\text{m}$, (d) Dec 15th, 2021, $H_s = 2.15\text{m}$, colored by hover. Black horizontal line is mean γ over surf zone.

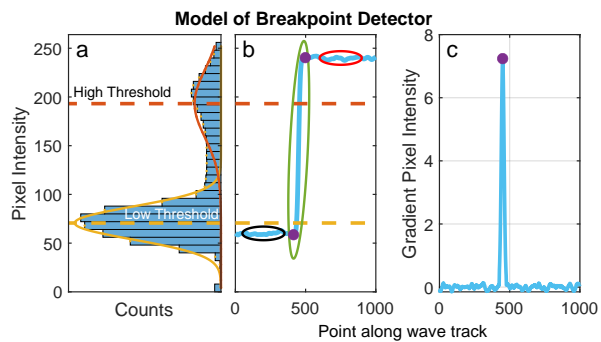


Figure 11: Schematic of breakpoint location using gradients of pixel intensity. (left) histogram of pixel intensity of the full image (10^7 counts are shown) typically have two maxima and each is fit to a Gaussian distribution, centered around high and low thresholds (red and yellow respectively). (middle) idealized pixel intensity versus location on wave track segment completely within (all broken) or completely seaward (unbroken) of surf zone (red and black circles, respectively). Sharp gradients (green) indicate breakpoint. (right) idealized pixel intensity gradient versus along-track location.